Article

Landslide Risk Assessment Using a Combined Approach Based on InSAR and Random Forest

Wangcai Liu [1], Yi Zhang [1,*], Yiwen Liang [1], Pingping Sun [2], Yuanxi Li [1], Xiaojun Su [3], Aijie Wang [1] and Xingmin Meng [1]

1   Technology & Innovation Centre for Environmental Geology and Geohazards Prevention, School of Earth Sciences, Lanzhou University, Lanzhou 730000, China; liuwc20@lzu.edu.cn (W.L.); liangyw19@lzu.edu.cn (Y.L.); liyq2021@lzu.edu.cn (Y.L.); wangaj21@lzu.edu.cn (A.W.); xmmeng@lzu.edu.cn (X.M.)
2   Key Laboratory for Geo-Hazards in Loess Area, Ministry of Natural Resources, Xi'an Center of Geological Survey, China Geological Survey, Xi'an 710054, China; sunpingping203@gmail.com
3   College of Earth and Environmental Sciences, Lanzhou University, Lanzhou 730000, China; suxj19@lzu.edu.cn
*   Correspondence: zhangyigeo@lzu.edu.cn

Abstract: Landslide risk assessment is important for risk management and loss–damage reduction. Herein, we assessed landslide susceptibility, hazard, and risk in the urban area of Yan'an City, which is located on the Loess Plateau of China and affected by many loess landslides. Based on 1841 slope units mapped in the study area, a random forest machine learning classifier and eight environmental factors influencing landslides were used for a landslide susceptibility assessment. In addition, differential synthetic aperture radar interferometry (DInSAR) technology was used for a hazard assessment. The accuracy of the random forest is 0.903 and the area under the receiver operating characteristics (ROC) curve is 0.96. The results show that 16% and 22% of the slope units were classified as being at very high and high-susceptibility levels for landslides, respectively, whereas 16% and 24% of the slope units were at very high and high-hazard levels for landslides, respectively. The landslide risk was obtained based on the susceptibility map and hazard map of landslides. The results show that only 26% of the slope units were located at very high and high-risk levels for landslides and these are mainly concentrated in urban centers. Such risk zones should be taken seriously and their dynamics must be monitored. Our landslide risk map is expected to provide information for planners to help them choose appropriate locations for development schemes and improve integrated geohazard mitigation in Yan'an City.

Keywords: landslides; risk assessment; random forest; DInSAR; Yan'an city

1. Introduction

Landslides are common natural phenomena on mountains and slopes that can change the geomorphology of the landscape. Thus, the massive destruction caused by landslides is of great concern [1,2]. With global climate change and increasingly intense human engineering, landslides tend to occur more frequently, resulting in huge economic losses and many casualties [3,4]. Therefore, risk assessment is often the focus of research [5–8], especially in populated areas that are prone to landslides. This should help provide the necessary information to governments and decision makers [6,9]. Risk assessment is the basis for risk management. It refers to the possibility and severity of landslides impacting life, health, property, and the environment. In practice, the risk of landslides is computed as the product of landslide hazard and the vulnerability to potential value loss [5]. Quantitative and accurate risk assessment can be effective information for government departments in land and resources planning, engineering construction, the prevention and early warning of landslides, and sustainable development.

It is crucial to select an optimal model and methodology for landslide risk assessment because different assessments may have different results and accuracies for the same areas. In recent decades, numerous landslide susceptibility, hazard, and risk assessment methods have been applied. However, there has been no study showing that a certain model has the optimal solution for all risk assessments [10,11]. Models for landslide susceptibility assessment can be classified as physically deterministic, heuristic based on experts' knowledge, and data-driven quantitative [12]. Physically deterministic models are commonly based on hydrological characterizations combined with infinite-slope stability analyses to estimate the relative stability of slopes [13]. Some research has pointed out that these models are used only for particular hydrological conditions and high model preconditions [14], such as detailed and homogeneous soil mechanical parameters, hydro environmental factors, and simple landslide types. For this reason, they could be effective only for mapping small areas in detail [15,16]. Heuristic models based on experts' knowledge, including the analytical hierarchy process (AHP) [17], expert knowledge systems [18], and gray relational modes [18], mainly rely on constructing a relatively simple ranking method determined by experts' knowledge [16]. Although heuristic models have the advantages of easy application, the assessment results have low accuracy with a certain level of subjectivity [19]. Previous studies show that data-driven quantitative models are preferred and applied more frequently than qualitative evaluation models, such as heuristic or geomorphological mapping [20,21]. Logistic regression (LR) [22,23], frequency ratio (FR) [24,25] and weights of evidence [26] are the most frequently used statistical models. They are based on considered classical statistics; index-based, machine learning; neural networks; and multi-criteria decision analysis. In particular, the use of machine learning for landslide assessment is rapidly increasing [20]. It is a modeling methodology that builds complex relationships between data and target variables through iterative training and learning without assuming additional structural constraints [27,28]. Machine learning is often used to solve nonlinear geological environment problems, such as landslide susceptibility assessment and prediction. For example, Chen et al. [29] introduced a new bivariate statistical-based kernel logistic regression to obtain landslide susceptibility maps by optimizing different kernel functions and two-component statistical correlation analyses. Behnia et al. [30] produced susceptibility maps for debris flows and other geohazards along the Yukon Alaska Highway Corridor, in Canada. Hong et al. [31] built a higher-precision susceptibility map of the Guangchang area in China based on a decision tree model. Furthermore, many studies have compared the accuracy of machine learning with classical statistical models in landslide susceptibility assessment [32–34]. They showed that machine learning models provide more accurate assessments and predictions [35].

Apart from models and methods, selecting appropriate mapping units associated with the research purpose is a key issue for reasonable and accurate assessment maps. Generally, the mapping units fall into several groups: grid cells, terrain units, unique conditional units, topographic units, slope units, complementary geohydrological units and political or administrative units [20,36]. Each type of unit has certain analytical advantages and disadvantages. For this reason, the type of unit needs to be determined at the beginning of a study according to the purpose and scale of the research [36,37]. Landslides tend to show a clear shape and boundary soon after their occurrence so the slope unit is often preferred for representing the form of landslides or unstable slopes. In some studies, the slope unit also performed better than the pixel unit in landslide assessment [38–40].

Yan'an, which is located in the north of Shaanxi Province, on the Loess Plateau, is a typical valley city. Its particular geography and geological environment background, as well as increasing human engineering activities, appear to be the causes of more frequent landslides, collapses, and other geohazards [41]. Several studies have evaluated the susceptibility and stability of landslides in Yan'an City and Baota District based on qualitative methods and physical models [42–44]. However, the evaluation factors in those studies are limited to geological or topographic conditions, and few studies have focused on the deformations which can reflect the activity of slopes through SAR data in the risk assess-

ment of the study area. Interferometric synthetic aperture radar (InSAR) technology can be used to optimize the landslide susceptibility assessment and reduce landslide classification errors [45]. Additionally, a smaller range and larger scale of quantitative assessments are necessary for future urban development in Yan'an City if we want to mitigate the geohazards occurring in current urban constructions. Therefore, this study aims at constructing a detailed landslide risk assessment in Yan'an City using high-resolution aerial images and a digital elevation model (DEM). A detailed investigation and understanding of the characteristics of the geological hazards in the urban area of Yan'an City is considered a critical part of risk assessment. In the process, it becomes necessary to combine ground deformation using InSAR technology with conventional topographic and geomorphic factors for risk analysis. Advanced random forest machine learning classifiers and InSAR technology are used in our study to assess landslide susceptibility, landslide hazards, and the identification of areas exposed to a higher landslide risk in the urban parts of Yan'an City. It is expected that the assessments of urban hazards and risks in urban areas based on the slope units can provide more accurate information for government departments and decision makers in urban planning, construction, and disaster prevention as well as control.

2. Study Area

The present study area is the central urban area of Yan'an City, which is located in the northern part of Shaanxi Province, China, on the Loess Plateau between the latitudes of 36°27′N and 36°41′N and the longitudes of 109°22′E and 109°33′E, covering an area of 185 km^2 (Figure 1). Its landform features typical and complex loess beams, mounds, and gullies. The highest elevation in the study area is 1300 m and the lowest elevation is 927 m, which is in the river valley, so the elevation difference is about 370 m. The climate in the area is semi-humid and semi-arid, with a continental monsoon climate. In the past, the average annual precipitation in Baota District was 537 mm, which occurred mainly from June to September [46].
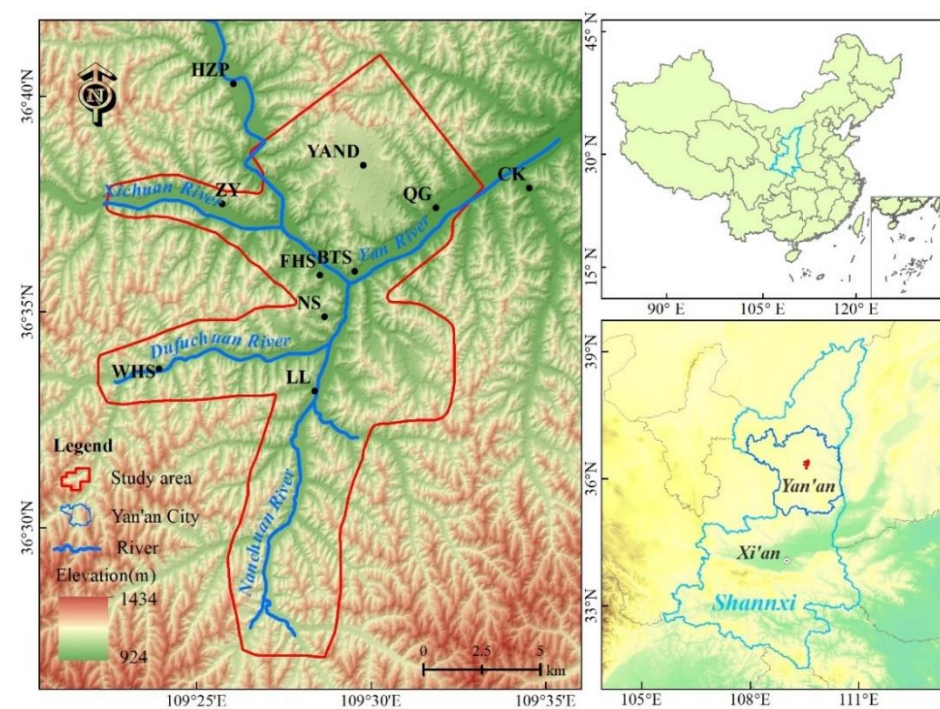

Figure 1. The location, boundary, and geomorphology of the present study area in Yan'an City and Shaanxi Province. YAND—Yan'an New District; HZP—Hezhuangping Town; QG—Qiaogou Street; CK—Chuankou Town; BTS—Baotashan Street; FHS—Fenghuangshan Street; ZY—Zaoyuan Town; NS—Nanshi Street; WHS—Wanhuashan Town; LL—Liulin Town.

From the perspective of regional geology and geotectonics, the study area is located in the middle-eastern part of the Ordos Block in the North China Block. The tectonic movement is slight without strong structural deformation and maintains the characteristics of a stable sedimentary basin. The strata are mainly Mesozoic and Cenozoic, including Triassic, Jurassic, and Quaternary; however, the Quaternary loess is the most widely distributed [47]. Triassic and Jurassic strata are mostly seen along both sides of the valley. Although there is no strong tectonic movement and fault, many landslides have occurred and developed in the area due to the unique physical and mechanical properties of loess. Loess is characterized by high porosity, low bulk density, weak cementation, water sensitivity, collapsibility, structural joints, vertical joints, unloading cracks, and a soft layer structural plane. Under the area's special landform conditions, landslide hazards could be induced by summer rainstorms and human engineering activities, which seriously affect the sustainable development of the local economy and society.

3. Data and Methods

The methodology applied for landslide susceptibility, hazard, and risk assessment is shown as a flowchart in Figure 2. A detailed explanation is provided in the following subsections.
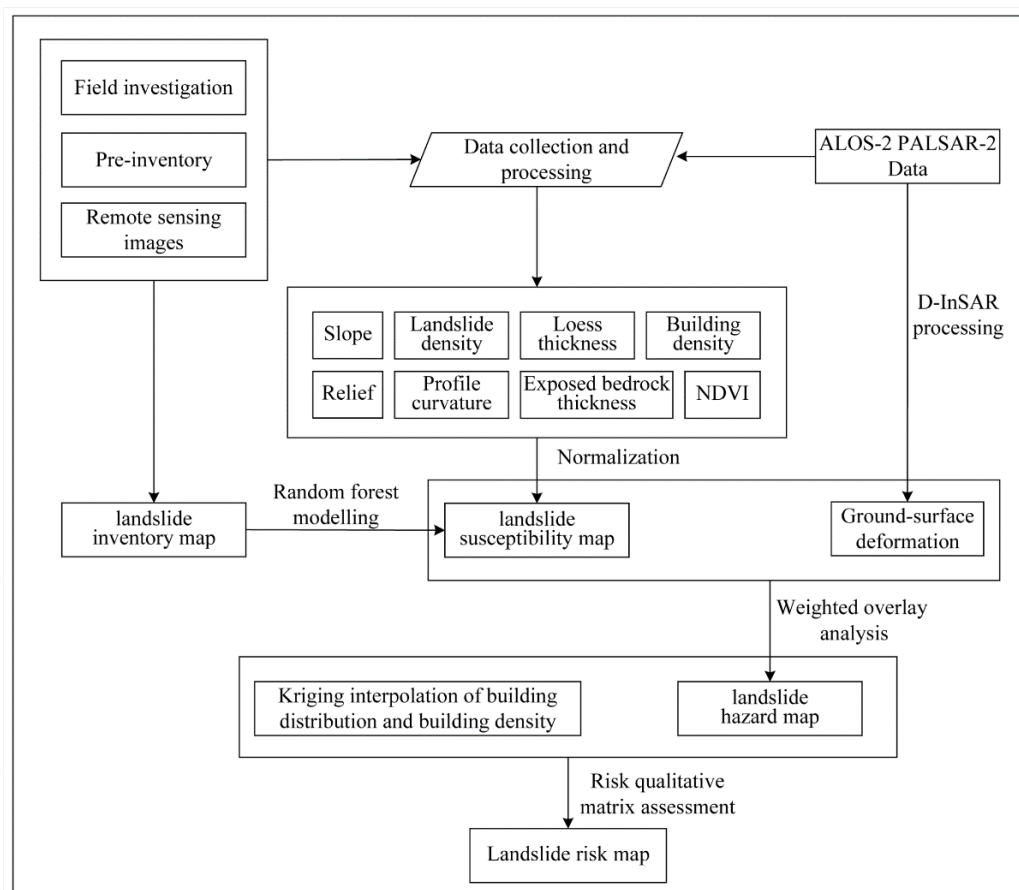

Figure 2. The flowchart of landslide risk assessment in the present study.

3.1. Landslide Inventory

A landslide inventory map is the first step to assess susceptibility. It shows information on all historical and active landslides. Combined with field surveys, relevant literature records and news reports of landslide records were used in this study to verify the spatial distribution of landslides using Google Earth high-resolution images and an unmanned aerial vehicle's digital orthophoto map (DOM) (0.1 m) provided by the Xi'an Center of China Geological Survey for visual interpretation.

Generally, slope units are defined by topographic characteristic lines (such as ridgelines and gully lines) and waterway paths, which are closely related to the DEM of the mountain area [36]. Therefore, these topographic characteristic lines and waterway paths are also the basic means to determine slope units in this study. Additionally, to better reflect the terrain of landslides or unstable slopes, we divided slope units according to topographic and geomorphic characteristics in the detailed field surveys. The basic requirement in a field survey is that every gully and slope must be investigated and the results are presented in the form of slope units. In this study, a total of 1841 slope units covering the whole study area were surveyed and the location and boundary of discernible slope units were obtained by the geographic information system (GIS) (Figure 3a). According to the current morphological characteristics and active state of the slopes in the field investigation, the slope units were divided into loess landslides, unstable slopes, and slopes to be evaluated. Loess landslides are the main historical landslides in the study area; unstable slopes show some deformation signs, such as creep slip, collapse, toppling, etc., and are developing toward becoming potential landslides. Finally, the landslide inventory map of the study area was aggregated and shown in Figure 3b, including 344 loess landslides and 411 unstable slopes, detailed in Section 4.1.
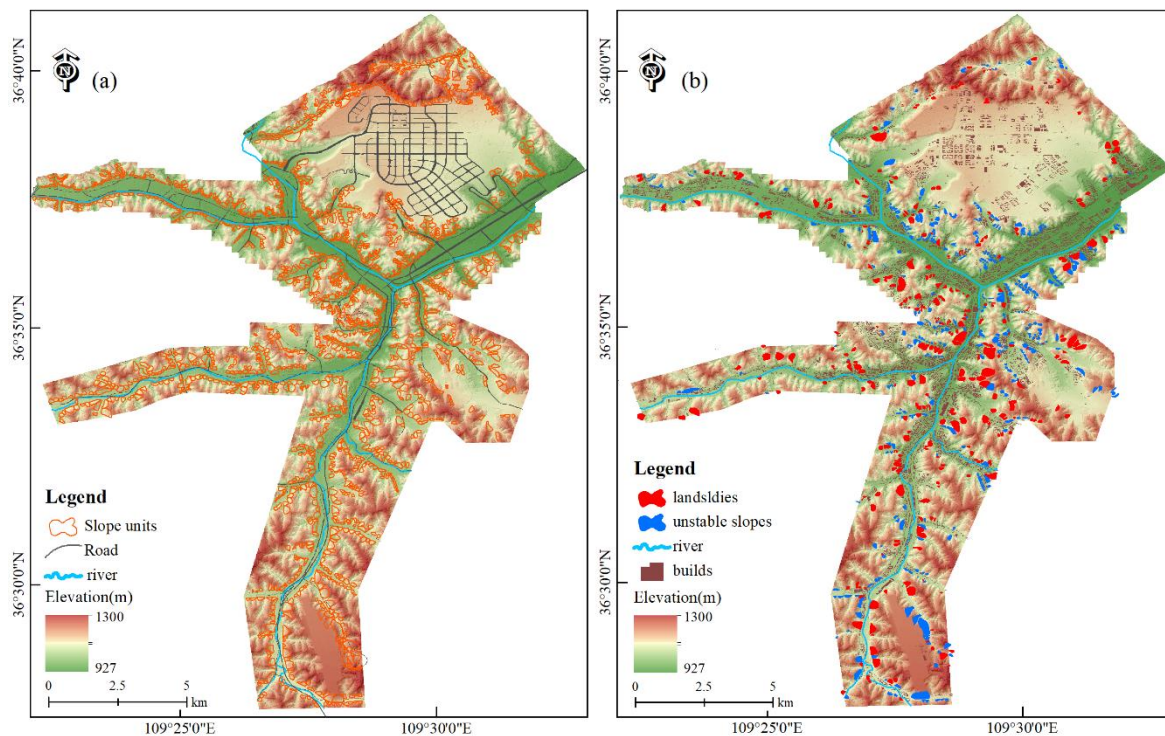

Figure 3. The inventory map of the present study. (**a**) Slope unit mapping and road elements based on topography and field surveys. (**b**) The distribution of landslides and unstable slopes in the study area.

3.2. Factors Influencing Landslides

Selecting appropriate environmental factors and inducing factors is the basis of risk assessment, which depends on data availability, scale, and study area, and affects future predictions [21,48]. Based on the field survey and previous work on landslides in the study area, we considered eight factors: slope, profile curvature, relief, the normalized difference vegetation index (NDVI), landslide density, building density, the thickness of loess, and the thickness of exposed bedrock. They are described below.

- Slope and profile curvature: A slope gradient is the measurement of the steepness of a surface. If the slope is too low, the gravitational potential energy is insufficient, and if the slope is too high, the material accumulation cannot provide the material basis for landslides. A profile curvature is used to describe the complexity of the terrain,

which is divided into convex, straight, and concave profiles, and reflects convergent and divergent drainages in addition to variations in erosion rate [49]. In the study, the slope and profile curvature were calculated using ArcGIS and a DEM with a spatial resolution of 2 m (Figure 4a,b).
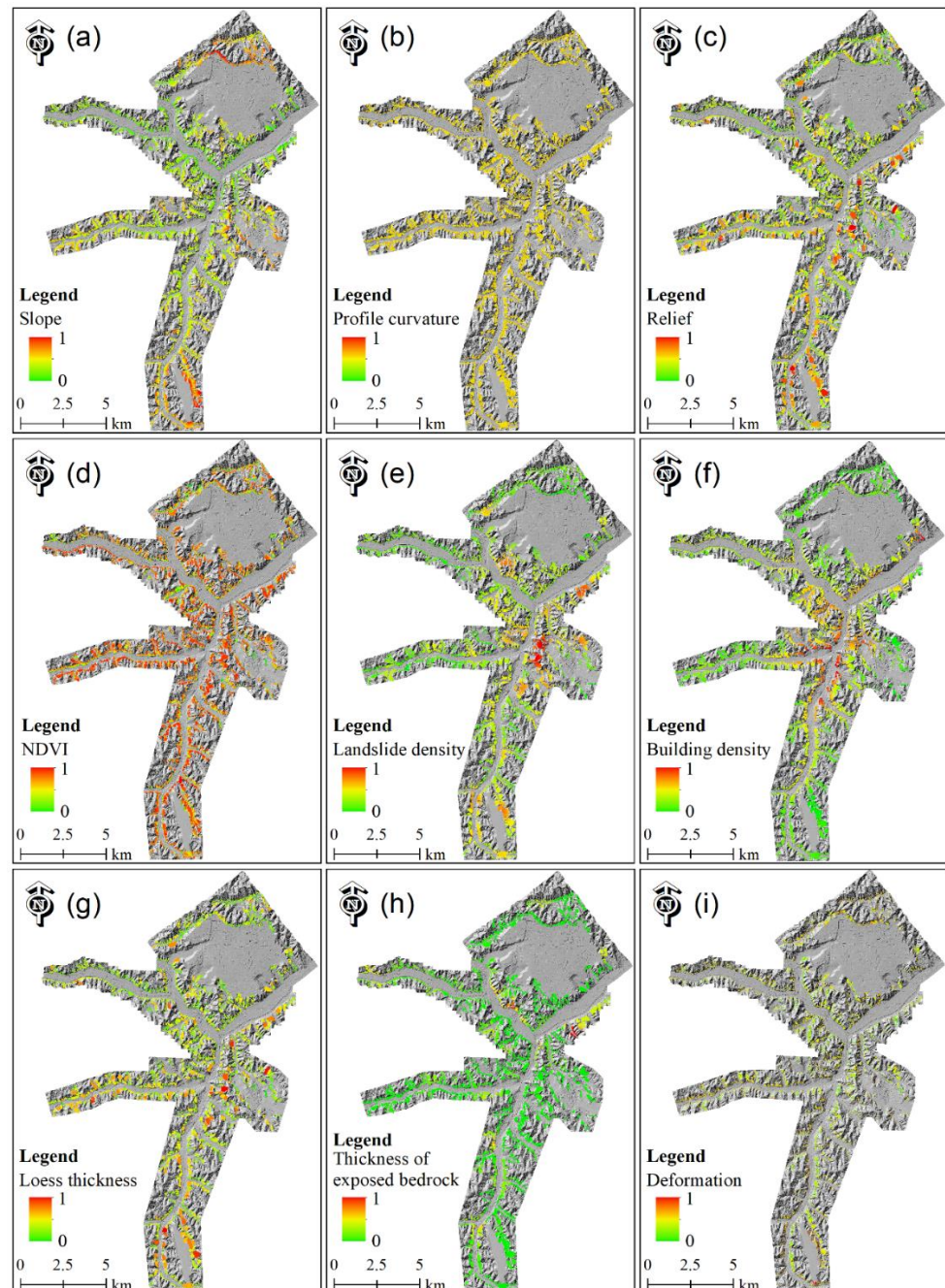

Figure 4. The conditioning factors used in this study: (**a**) slope; (**b**) profile curvature; (**c**) relief; (**d**) NDVI; (**e**) landslide density; (**f**) building density; (**g**) loess thickness; (**h**) thickness of exposed bedrock; and (**i**) deformation. The above parameters have been normalized.

- Relief: A relief represents the elevation difference within a certain range of the slope and determines the gravitational potential energy. Only enough gravitational potential energy can cause landslides (Figure 4c).
- NDVI: The NDVI reflects the vegetation cover in the study area. High vegetation coverage is needed to stabilize the slope by the root system and reduce the devel-

opment of landslides [50]. The NDVI value was calculated using the expression NDVI = (NIR − R)/(NIR + R) from Landsat-8 images, where NIR is the reflectivity of the near-infrared portion of the electromagnetic spectrum and R is the reflectivity of the red portion of the electromagnetic spectrum (Figure 4d).

- Landslide density and building density: The landslide density directly reflects the development quantity of disasters in an area. In urban areas, construction activity is one of the most dominant human activities that cause slope instability. Settlement along slopes in urban areas is an important factor in slope failure. Therefore, we used building density to reflect the effect of human activities on slope stability. Landslide density and building density were calculated for the slope units by vectorizing landslides and building contours and then interpolating them into grid data (Figures 3 and 4e,f).

The thicknesses of the loess and the exposed bedrock were measured during field investigations (Figure 4g,h). The loess thickness on a hillslope, which coincides with the failure depth, is a critical parameter in performing the slope stability analysis. The overlying loess thickness plays an important role in hydrological effects, such as the ratio of the saturated depth to the losses [51]. The thickness of the exposed bedrock of the slope has a great impact on the landslide scale, landslide type, and slope deformation [52]. Due to the undeveloped tectonic activity in the study area, the effect of earthquakes and faults has not been considered in this study. In addition, because precipitation within the relatively small study area is mostly unvarying, precipitation data were excluded from the analysis processes.

A statistical description of the influencing factors is shown in Table 1. To eliminate the dimensional influence of factors, the minimax normalization method was applied [53]. The continuous factor values of each factor were normalized, so all the values fall in the (0, 1) interval, where the normalized data were calculated following the equation below:

$$X_i' = \frac{x_i - x_{min}}{x_{max} - x_{min}} \tag{1}$$

where X_i' is the normalized input and x_i, x_{min}, and x_{max} are the actual, minimum, and maximum input data, respectively. The results of normalized factors are shown in Figure 4.

Table 1. Statistical description of the influencing factors.

Factors	Min	Max	Standard Deviation
Slope (°)	0	86.8	15.5
Profile curvature	−497.4	499.0	33.6
Relief (m)	8	166.6	29.4
NDVI	−0.23	0.98	0.18
Landslide density	0	0.27	0.06
Build density	0	0.22	0.04
Loess thickness (m)	8.0	160.2	29.3
Bedrock thickness (m)	0	24.5	3.4
Deformation (m)	0.11	−0.09	0.014

3.3. DInSAR

In general, the displacement of a pixel is calculated using the interference phase difference between two SAR images by using the pixel product of a reference image and slave image—this is the basic principle of InSAR [54]. DInSAR is applied to the removal of the topographic phase contribution from the interferogram deformation phase using a two-pass, three-pass, or four-pass technique; however, it is worth noting that the two-pass technique, which imports an external DEM, yields a more reliable and operational outcome [54,55]. Furthermore, several limitations of InSAR technology must be considered at the beginning of use. One limitation is geometric distortion caused by topography, especially in mountainous areas with high elevations, which is affected by the look side of

radar observation modes [56]. Another limitation is the poor coherence, even incoherence of interferograms caused by diffuse vegetation, which is very obvious in the C-band Sentinel-1 images of the study area [57].

In this research, two ascending SAR images acquired from ALOS-2 on 5 November 2018 and 20 May 2019 were selected for interference calculations (Figure 5a and Table 2). Due to the relatively flat terrain of the study area, the SAR images from a single orbit can be used to detect and monitor the deformation of most of the slopes. The sensor of ALOS-2 can transmit and receive the L-band with strong penetrating ability and can capture the ground deformation under the dense vegetation. The external DEM for removing the topographic phase and geocoding is the 1-arc-second (~30 m) Shuttle Radar Topography Mission (SRTM) data from NASA. Ground deformation along the LOS (light-of-sight) of the Yan'an City area was obtained after registration and resampling, differential interference, coherence calculation, filtering and phase unwrapping, orbit refining, and reflattening in addition to geocoding. All of these were processed with the DInSAR tool of the SARScape software (Figure 5b). The normalized deformation factor image is shown in Figure 4i.
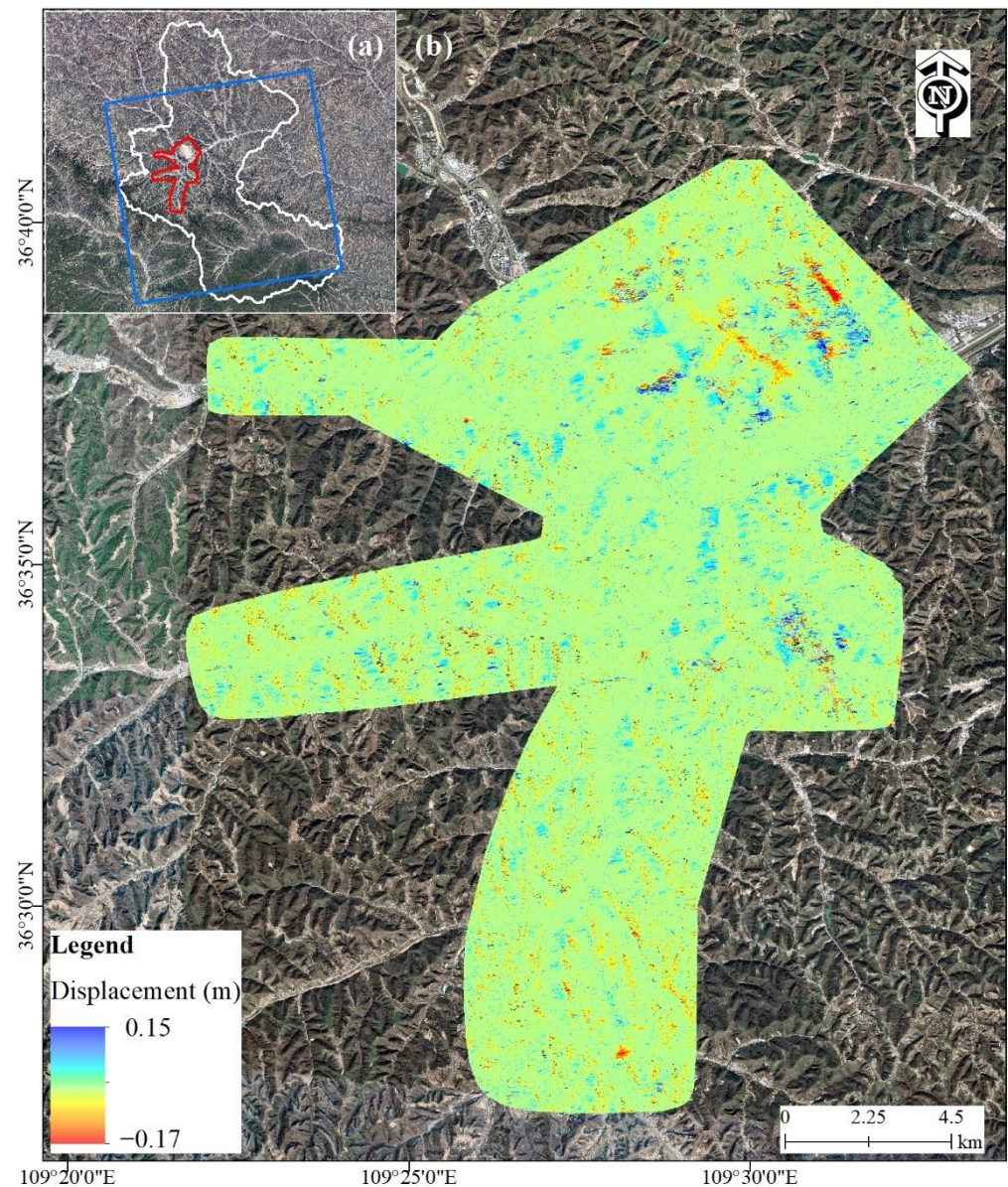

Figure 5. Area covered by two ascending SAR images from ALOS-2 (blue rectangle) in (**a**), and image of the LOS displacement of the study area (red polygon) using DInSAR technology in (**b**).

Table 2. Details of two SAR images and displacement from ALOS-2.

Sensor	PALSAR-2
Wavelength	23 cm
Band	L
Acquired time	5 November 2018 20 May 2019
Orbit direction	Ascending
Angle of incidence	32.5°
Polarization	HH
Observation mode	Fine
Resolution	10 m
Normal baseline	140.798 m
Absolute time baseline	196 days
Max displacement	0.150 m
Min displacement	−0.172 m
Standard deviation	0.018 m

3.4. Random Forest

Random forest has been widely used in data classification and management and has excellent performance in landslide susceptibility mapping. Random forest is an ensemble machine learning algorithm based on a decision tree. The classifier is a recursive process from root nodes to child nodes, which is similar to the combination of a decision tree and the flowchart of a tree structure [58]. The bootstrap method is used to extract multiple samples from the original samples. Starting from the nodes of a tree, the optimal features among different internal nodes are selected, and the corresponding branches are determined based on the test output. Finally, the results are obtained from the leaf nodes of the decision tree.

Random forest has strong generalization ability and can deal with multi-dimensional and large learning sets. Compared with other statistical learning models, random forest does not easily generate overfitting. It improves prediction accuracy without significantly increasing the amount of calculation. It has a higher tolerance for outliers and noise, resulting in data loss and imbalance. In this study, a random forest module was built based on the R language. Before running the random forest module to perform the landslide susceptibility assessment, the training and validation datasets must be selected. In the study, landslide inventories including stable slopes, unstable slopes, stable landslides, and unstable landslides were selected as training sites. Using ArcGIS, these slope units were converted into 109,981 vector points, where 3000 points were selected randomly at each of the landslide sites and non-landslide sites to train and test the classifier. Finally, its performance was evaluated with the ROC curve and confusion matrix.

4. Results

4.1. Characteristics of Landslides

Based on the field survey, the geohazards of Yan'an City were counted as 334 landslides, 411 unstable slopes, and land subsidence locations. Their depths of the sliding surface are mainly shallow (less than 30 m) [47]. The landslides can be classified as loess landslides and loess-bedrock interface landslides because most landslides occur in the loess layer or on the top of the bedrock (Figure 6a,b). The geometric morphology and characteristics of the loess landslides and the unstable slopes including the types, lengths, widths, height, slope angles, and others, such as the longitudinal shape and depth of slide surfaces, were mapped using the GIS and field investigations with high-resolution DEM (~2 m) (Table 3). The length and width of landslides are mainly in the range of 50 to 200 m. The height and slope angle are also condition factors of loess landslides. A higher or steeper slope has a higher degree of stress concentration and tensile stress range so it is more prone to failure and sliding. The study area is located in the loess hilly gully region with dense gullies, and the relative height differences of 60 to 150 m leads to the height of landslides usually being less than 120 m. Since the late Cenozoic era, the Loess Plateau has been in a

state of intermittent uplift, with rivers cutting sharply and ravines crisscrossing, creating topographic conditions for loess landslides. The longitudinal shape can control the values and positions of the stress inside the slope body and plays a key role in the stability. For example, flat and convex slopes tend to be more easily destroyed under stress, suggesting an unstable evolutionary trend, whereas sunken and stepped slopes tend to be more stable with less stress concentration. Therefore, the longitudinal shapes of landslides in this study are mainly flat and convex slopes.
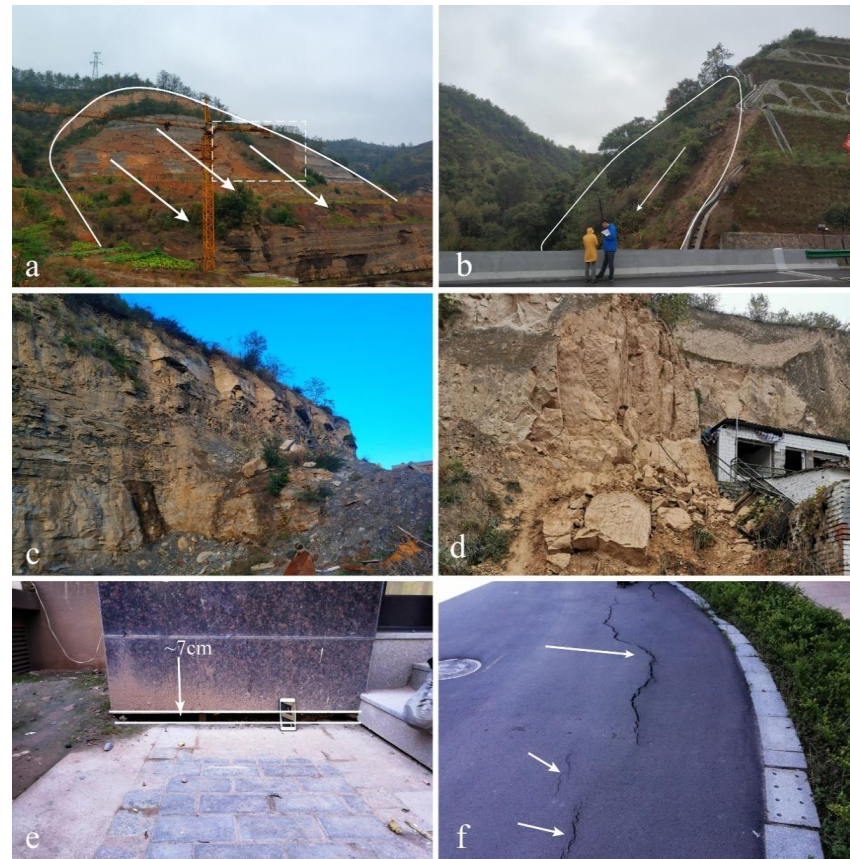

Figure 6. Examples of geohazard types mapped in the study area: (**a**) loess–bedrock interface landslide; (**b**) loess landslide; (**c**) soil–bedrock unstable slope; (**d**) soil unstable slope; and (**e**,**f**) cracks and damages in the ground and buildings due to land subsidence. Arrows indicate the direction of the slide and the location of the cracks.

Table 3. Types and characteristics of landslides and unstable slopes. L and U represent landslides and unstable slopes, respectively.

	Type		Length (m)		Width (m)		Height (m)		Slope (°)		Area (10³m²)	
L	Loess	243	<50	26	<50	25	≤30	7	≤20	10	≤5	73
			50–100	108	50–100	107	30–60	113	20–30	95	5–10	73
			100–150	104	100–150	99	60–90	118	30–40	174	10–15	59
			150–200	50	150–200	41	90–120	69	40–50	55	15–20	46
	Loess-bedrock	91	200–250	22	200–250	31	120–150	24	>50	0	20–25	17
			>250	24	>250	31	>150	3			25	66
U	Loess	285	≤50	76	≤50	35	≤30	19	≤20	12	≤5	145
			50–100	218	50–100	160	30–60	184	20–30	59	5–10	143
	Bedrock	5	100–150	82	100–150	138	60–90	161	30–40	231	10–15	61
			150–200	19	150–200	39	90–120	40	40–50	108	15–20	28
	Loess-bedrock	121	200–250	10	200–250	18	120–150	6	>50	1	20–25	12
			>250	6	>250	21	>150	1			>25	22

Unstable slopes refer to a slope with creep slip, collapse, toppling, lateral tensile fracture, and other deformation characteristics or trends, and that is regarded as a potential geohazard. The 411 unstable slopes from the field survey were divided into three types according to their material composition: (i) soil unstable slope, (ii) rock unstable slope, and (iii) soil–bedrock unstable slope. There were about 285 soil unstable slopes in the study area, accounting for 69% of the total number of unstable slopes. Soil–bedrock unstable slopes and rock unstable slopes are fewer, numbering 125 and five, respectively, accounting for 31% of the total number of unstable slopes and mainly occurring in the Quaternary loess and the Jurassic sandstone strata. The unstable slopes have similar characteristics to landslides in their ranges of length, width, height, and area but the slope angles of unstable slopes are relatively larger. The characteristics of landslides and unstable slopes in the present study are summarized in Table 3.

In addition, under the pressure of population growth and development as well as the preservation of historical and cultural sites, in 2012 the government built a new district called Yan'an New District by cutting mountains and filling ditches. However, because of the special microstructure and complex engineering-geological conditions of the loess, land subsidence in Yan'an New District has become one of the geohazards that requires much attention. The surface deformation along the radar LOS calculated by the DInSAR technique was very similar to that of the small baseline subsets InSAR (SBAS-InSAR) approach from Sentinel-1 images (see [59,60] for more details). DInSAR and field surveys show that the land subsidence area is the ribbon (Figure 7), mainly concentrated in the filling area manifested as wall cracking or collapse, ground subsidence, and cracks (Figure 6e,f).
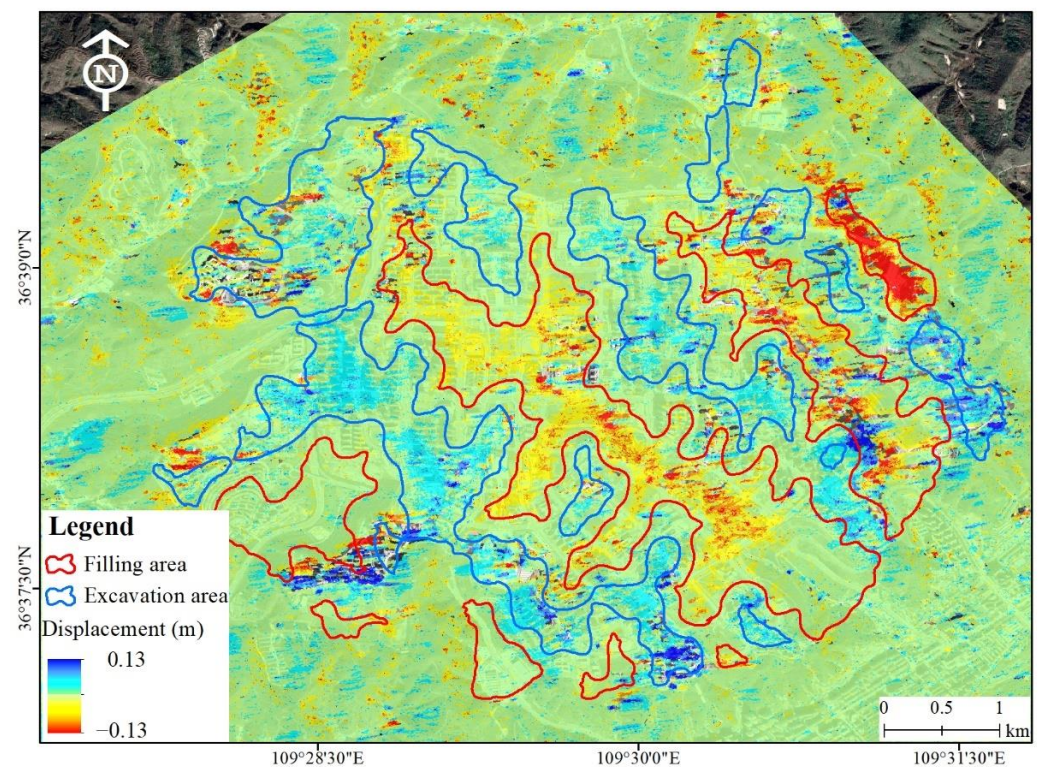

Figure 7. Surface deformation image of Yan'an New District from 2018 to 2019 calculated using DInSAR. Positive values indicate that the ground object deformation is close to the radar along the radar LOS, and negative values indicate that the ground object deformation is far away from the radar along the radar LOS.

4.2. Landslide Susceptibility Mapping

The normalized factors were used as the input, and the landslide susceptibility index was the output data. The mean decrease accuracy and mean decrease Gini coefficient of the

random forest are used to order the eight variables (Figure 8). The vertical axis represents the eight variables, with the mean decrease accuracy and mean decrease Gini coefficient decreasing from top to bottom. It shows that the importance of the hazard density is the highest and that the build density, thickness of exposed bedrock, loess thickness, relief, and the NDVI are the next most-important. The ROC curve is widely used to evaluate the classification results of the random forest classifier through the area under the ROC curve (AUC) [35]. The vertical axis and horizontal axis represent the true positive rate (TPR) and false-positive rate (FPR) using the random forest classifier, respectively. TPR and FPR, also called the sensitivity and specificity, are the ratio of the landslide sample points correctly detected by the classifier and the ratio of the non-landslide sample points incorrectly classified as landslide sample points, respectively [61]. The larger the AUC, that is, the closer the vertex of the curve is to the upper left corner, the better the classifier's test capability. In this research, the AUC is 0.96, which indicates excellent classification results of the random forest classifier (Figure 9). In addition, the confusion matrix shows that the overall accuracy of the random forest classifier is 0.903 and that the predicted precision of non-landslides and landslides is 0.927 and 0.881, respectively, which is a good method to analyze the prediction accuracy (Table 4). Four levels of susceptibility, i.e., very high (>0.711), high (0.711–0.458), moderate (0.458–0.231), and low (<0.231), were categorized based on the natural breaks classification conducted using the ArcGIS software (Figure 10). The natural breaks classification was determined based on natural groupings inherent in the data. Then, the classification interval was identified to provide an optimum grouping of similar values and maximize the differences between classes [62,63]. Additionally, the distribution of the landslide susceptibility index using the natural breaks is shown in Figure 10b.
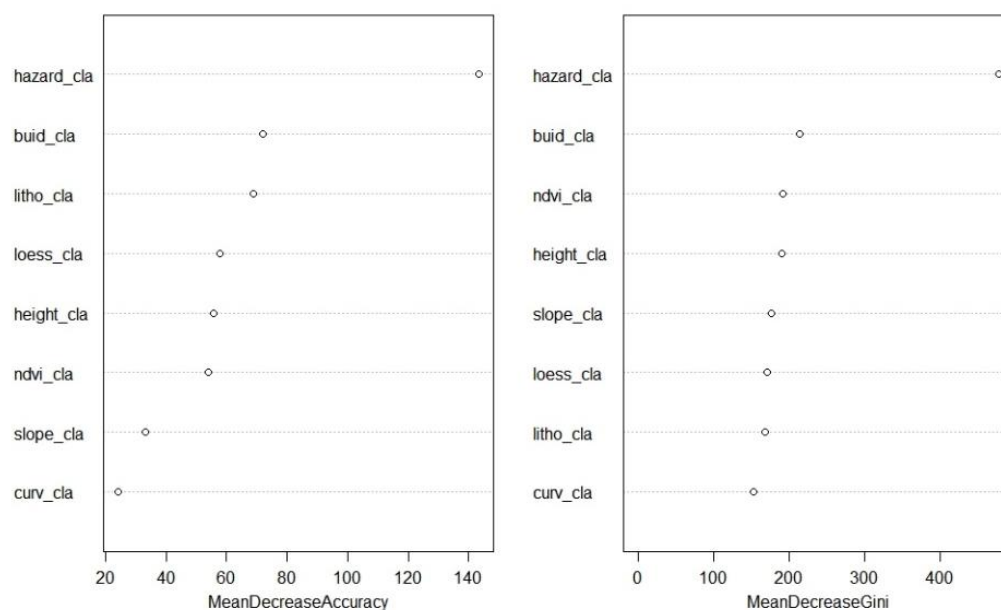

Figure 8. Mean decrease accuracy and mean decrease Gini of variables assigned by the random forest classifier. The vertical axis is the inducing factor variable. hazard—hazard density; build—build density; lithe—thickness of exposed bedrock; loess—loess thickness; height—relief; ndvi—NDVI; curv—profile curvature.

The results show that the distribution of landslides and unstable slopes in the study area is closely related to the susceptibility partitioning (Table 5). Over one-third of the slope units in the study area are in the high- and very high-susceptibility areas, accounting for 21% and 16% of the total, respectively, with a total area of 10.1 km^2; the remaining slope units are in the moderate- and low-susceptibility areas. Moreover, 35% of the landslides and the unstable slopes are located in the very high-susceptibility area, accounting for 16%

of the total number of the slope units; 33% of the landslides and the unstable slopes are located in the high-susceptibility areas, accounting for 21% of the total number of the slopes; 21% of the landslides and the unstable slopes are located in the moderate-susceptibility area, accounting for 27% of the total number of the slopes; and 11% of the landslides and the unstable slopes are located in the low-susceptibility areas, which account for 36% of the total number of slopes.
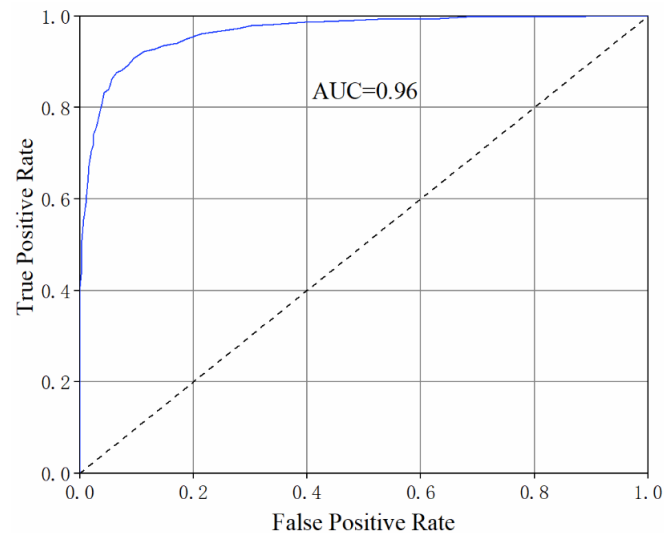

Figure 9. ROC curves and AUC value for evaluating the classification results of landslide susceptibility using the random forest classifier.

Table 4. Confusion matrix of the random forest classifier.

RF		Predicted		Recall
		Non-Landslide	**Landslide**	
Actual	Non-landslide	543	73	0.881
	Landslide	43	541	0.926
	Precision	0.927	0.881	0.903

The results of the landslide susceptibility assessments show that two regions are highly prone to landslides, one being the urban center of Baota District, and the other Nanniwan Airport (Nnwa) and its surrounding areas. In the urban center of Baota District, including Yangjialing Village (Yjl), Nanshi Street (Ns), Baiping Village (Bp), Hutoumao Village (Htm), Zezigou Village (Zzg), Nanzhaibian Village (Nzb), Majiawan Village (Mjw), Huanghaowa Village (Hhw), Mata Village (Mt), Erzhuangke Village (Ezk), and Shanlangcha Village (Slc), where landslides occur frequently, the landslide susceptibility is high and very high because of the very high-density population and frequent human activities (Figure 10). Due to the effects of road construction, domestic water discharge, crop planting, slope toe excavation, and other activities, landslides, including rock falls, slope failures, unstable slopes, and creep, occur frequently, which poses a great threat to the lives and properties of the local residents. The other highly landslide-prone areas are Nanniwan Airport (Nnwa) and its surrounding areas, including Yangjiawan Village (Yjw), Maozegou Village (Mzg), Sanshipu Village (Ssp), and Yejiagou Village (Yjg). Nnwa is the area of mountain excavation and valley infilling on the Loess Plateau and its construction destroys the stability of the surrounding slopes, resulting in the development of landslides and unstable slopes in the surrounding areas.
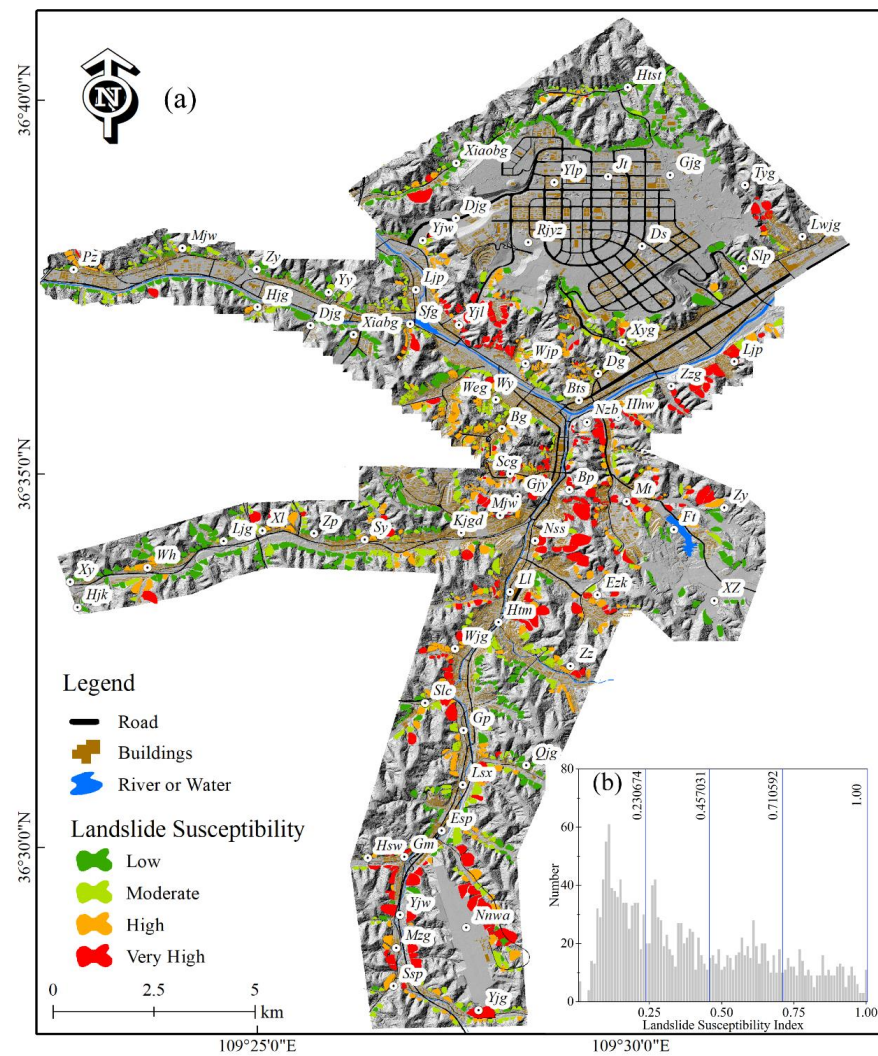
Figure 10. Landslide susceptibility map of the study area in (**a**), and the distribution of the landslide susceptibility index using the natural breaks in (**b**).

Table 5. Slope unit statistics based on landslide susceptibility, hazard, and risk zone.

	Slope Units	VH	H	M	L
Susceptibility zone	Number	291	401	495	654
	Total areas	5.8	4.3	4.6	6.9
	Proportion (N)	16%	22%	27%	36%
	Landslides	122	96	62	54
	Unstable slopes	138	147	96	30
Hazard zone	Number	293	439	583	526
	Total areas	6.4	4.7	6	4.5
	Proportion (N)	16%	24%	32%	29%
	Landslides	123	89	77	45
	Unstable slopes	131	149	93	38
Risk zone	Number	116	377	560	788
	Total areas	2.0	4.4	6.0	9.2
	Proportion (N)	6%	20%	30%	43%
	Landslides	55	78	99	102
	Unstable slopes	41	132	133	105

4.3. Landslide Hazard Mapping

Reliable landslide hazard mapping is crucial for hazard mitigation and risk management. In this study, InSAR technology was used to obtain the landslide hazard assessment, aiming for an ongoing and quantitative practice [63]. The fieldwork showed that the landslide type in the study area was relatively single, mainly loess landslides, and that the geological environment and inducing conditions, such as rainfall, are similar in the small study area, leading to the relatively simple mechanism of loess landslide activity. Therefore, DInSAR was used as a comprehensive indicator to reflect slope displacement, whether caused by rainfall or human activities, in landslide hazard assessment. The spatial probability of landslides (landslide susceptibility) and the intensity of ground surface deformation were used in the weighted overlay model parameters to calculate landslide hazard [64]. The weighted overlay technique is defined to develop a map using the overlays of several raster layers by giving weight to each raster layer according to expert opinions [65]. The weighted overlay analysis was applied to obtain the landslide hazard assessment using the following equation:

$$WX_i = \sum_{j=1}^{m} R(j) \times X(i,j) \tag{2}$$

where *m* is the total number of factors to assess, WX_i is the hazard index of the assessment units, $R(j)$ is the weight value of each factor, and $X(i,j)$ is the value of the assessment factors. In this study, $X(i,j)$ is the landslide susceptibility index obtained from the random forest and the ground–surface deformation intensity that was defined using the normalized ground deformation data obtained from DInSAR during the monitored time; the weight values of both were set at 0.5 after analyzing the geological environment and inducing conditions of landslides in the study area, respectively. Finally, the hazard indexes of slope units were calculated by summing the product of assessment factors and corresponding weight values. Four levels of hazard, i.e., very high (>0.594), high (0.594–0.416), moderate (0.416–0.269), and low (<0.269), were categorized based on the natural breaks classification, and the LOS displacement in different hazard levels were counted, which are illustrated in Figures 11 and 12, respectively.

The number and LOS displacement values of slope units in different hazard levels are illustrated in Figure 11. The distribution histogram shows the maximum and mean displacement values, as well as the number of slope units in different hazard levels. It shows that the displacement values of slope units are distributed in a normal curve and that the higher hazard of slope units presents a higher displacement value than the lower hazard on the whole. The results show that 40% (732) of the slope units in the study area are in the high- and very high-hazard areas for landslides, accounting for 24% and 16% of the total, respectively, with a total area of 11.1 km^2 (Figure 12). There was a small increase in the number and distribution of the hazard zones in the urban areas compared with the susceptibility map. About 34% (254) of the landslides and the unstable slopes are located in the very high-hazard areas, accounting for 14% of the total number of slopes; 32% (234) of the landslides and the unstable slopes are located in the high-hazard areas, accounting for 13% of the total number of slopes; 23% (170) of the landslides and the unstable slopes are located in the moderate-hazard areas, accounting for 9% of the total number of slopes; and 11% (83) of the landslides and the unstable slopes are located in the low-hazard areas, which are 5% of the total number of slopes. The results show that the spatial distribution of landslide hazard areas was consistent with the field investigations.
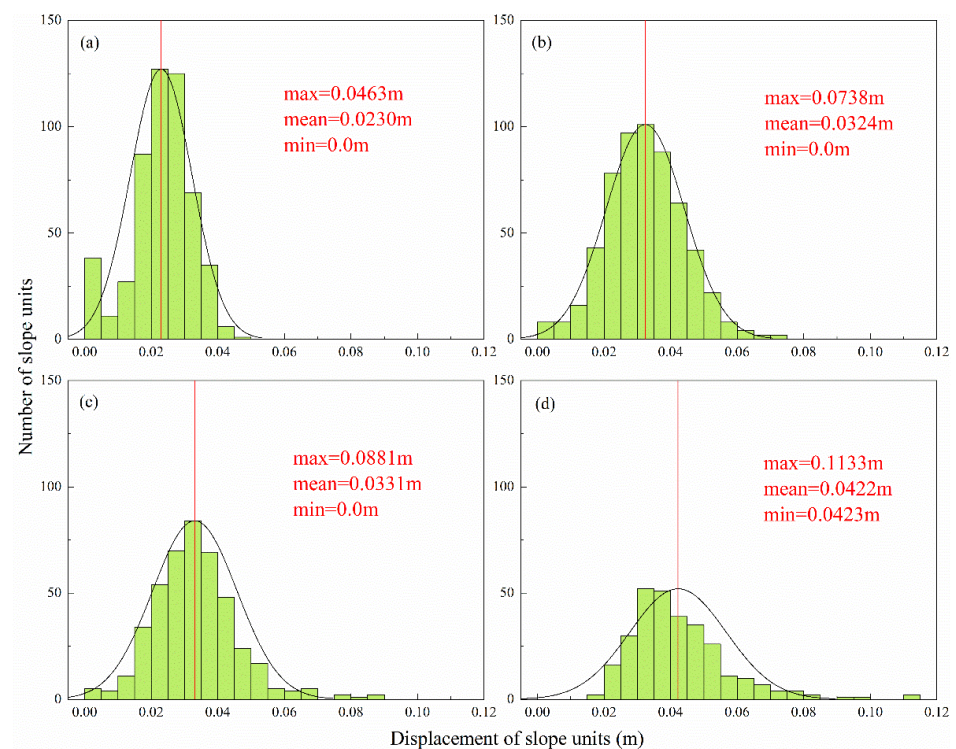
Figure 11. Distribution histogram of the number and LOS displacement values of slope units in different hazard levels: (**a**) low hazard; (**b**) moderate hazard; (**c**) high hazard; and (**d**) very high hazard. The red lines represent the average displacement values in different hazard levels.

4.4. Landslide Risk Mapping

The JTC-1 Joint Technical Committee on Landslides and Engineered Slopes noted that landslide risk is a measure of the probability and severity of the adverse effects of landslides on health or property, which must consider the hazard mapping and vulnerability of landslides [5]. Vulnerability assessment is a fundamental element in the evaluation of landslide risks [66]. Vulnerability to landslides is expressed in economic (monetary, quantitative) and heuristic (qualitative) scales. When using economic measurements, vulnerability is commonly expressed in the element values, such as monetary, intrinsic, and utilitarian values [67]. Due to a lack of information about properties and population distribution data, the Kriging interpolation of building distribution and building density was used for the vulnerability assessment in this study. The location and spatial distribution of buildings reflect the distance between buildings and slope units, which indirectly indicates the extent to which buildings and populations are threatened by landslides. Additionally, the building density can also indicate the properties and populations. Of course, this assumes that the sizes and values of the buildings are similar and that the differences in the populations attached to the different buildings are slight. The equation for landslide risk calculation is expressed as follows:

$$R = H_L \times V_L \tag{3}$$

where H_L and V_L represent the landslide hazard and vulnerability, respectively. The landslide risk index obtained from Equation (3) is divided into four levels according to the natural breaks method after normalization, namely, very high-risk (>0.406), high-risk (0.406–0.223), middle-risk (0.223–0.101), and low-risk (<0.101). The results of the risk assessment zones and statistics are shown in Figure 13 and Table 5.
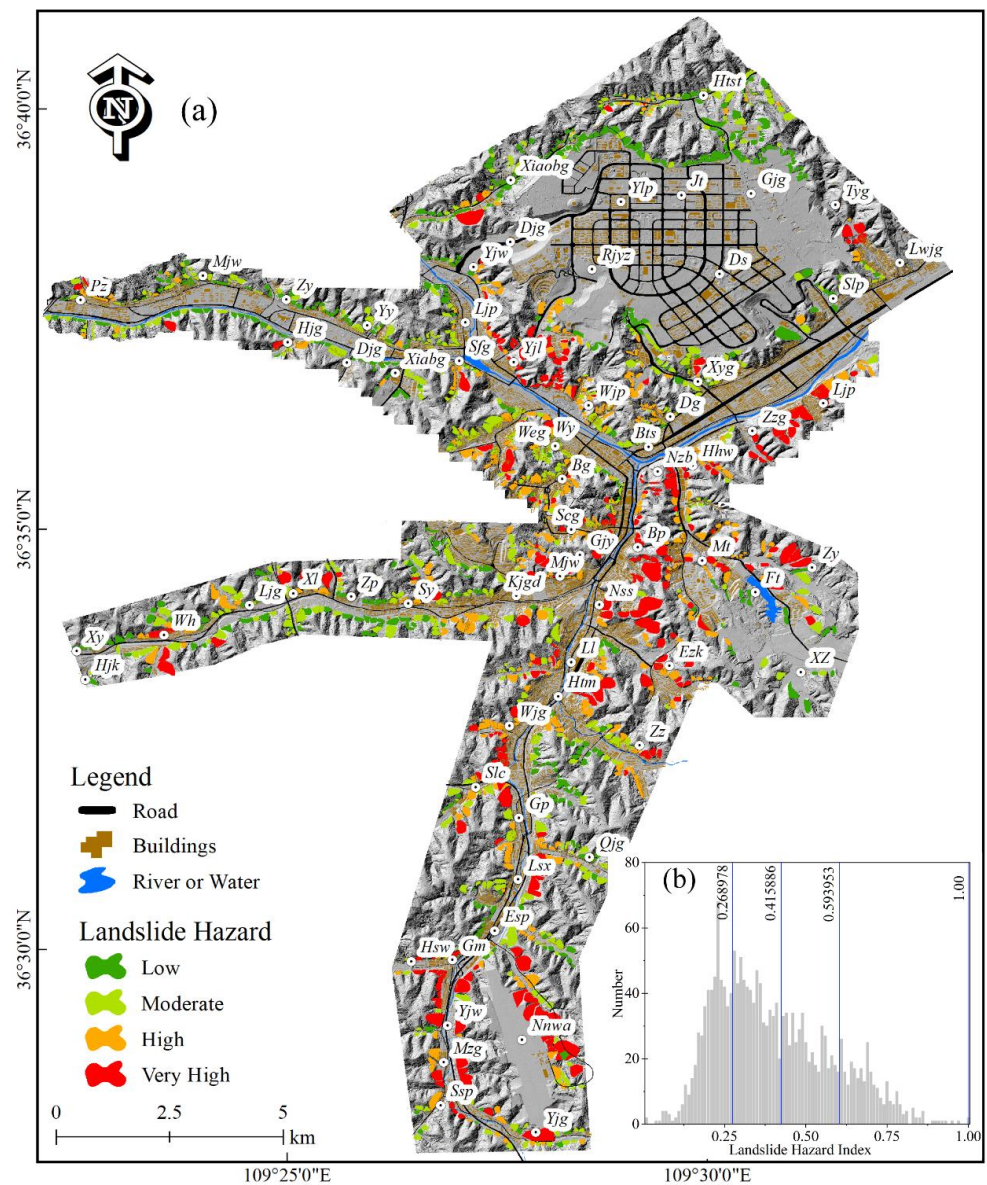
Figure 12. Landslide hazard map of the study area in (**a**), and the distribution of landslide hazard index using the natural breaks in (**b**).

The landslide risk assessment map shows that the risk in the urban center is higher than that in the suburban areas, where the risk decreases with increasing distance from the urban center (Figure 13). Additionally, a total of 20 and 167 extra slopes are in very high and high-hazard zones besides landslides and unstable slopes (Table 5). About 6% (116) of the slope units are located in very high-risk zones with a total area of about 2 km^2; 20% (377) of the slope units are located in high-risk zones with a total area of about 4.4 km^2, which are mainly distributed in concentrated areas (i.e., Yjl-Sy-Slc-Hhw) (Figure 13 and Table 5). The building and population densities in these areas are high, which may lead to significant economic losses and casualties, so it is necessary to pay more attention and conduct landslide risk management to mitigate the landslide risks. Compared with the landslide susceptibility and hazard maps, Nnwa and its surrounding areas are classified into moderate- and low-risk areas because of the low population density in the areas. In addition, many engineering solutions, including slope geometry modification, underground drainage systems, gravity retaining walls, and anti-slide piles, have been applied to stabilize the slopes. Therefore, the slopes, which are originally very highly prone to landslides, are classified as low-risk zones for landslides.
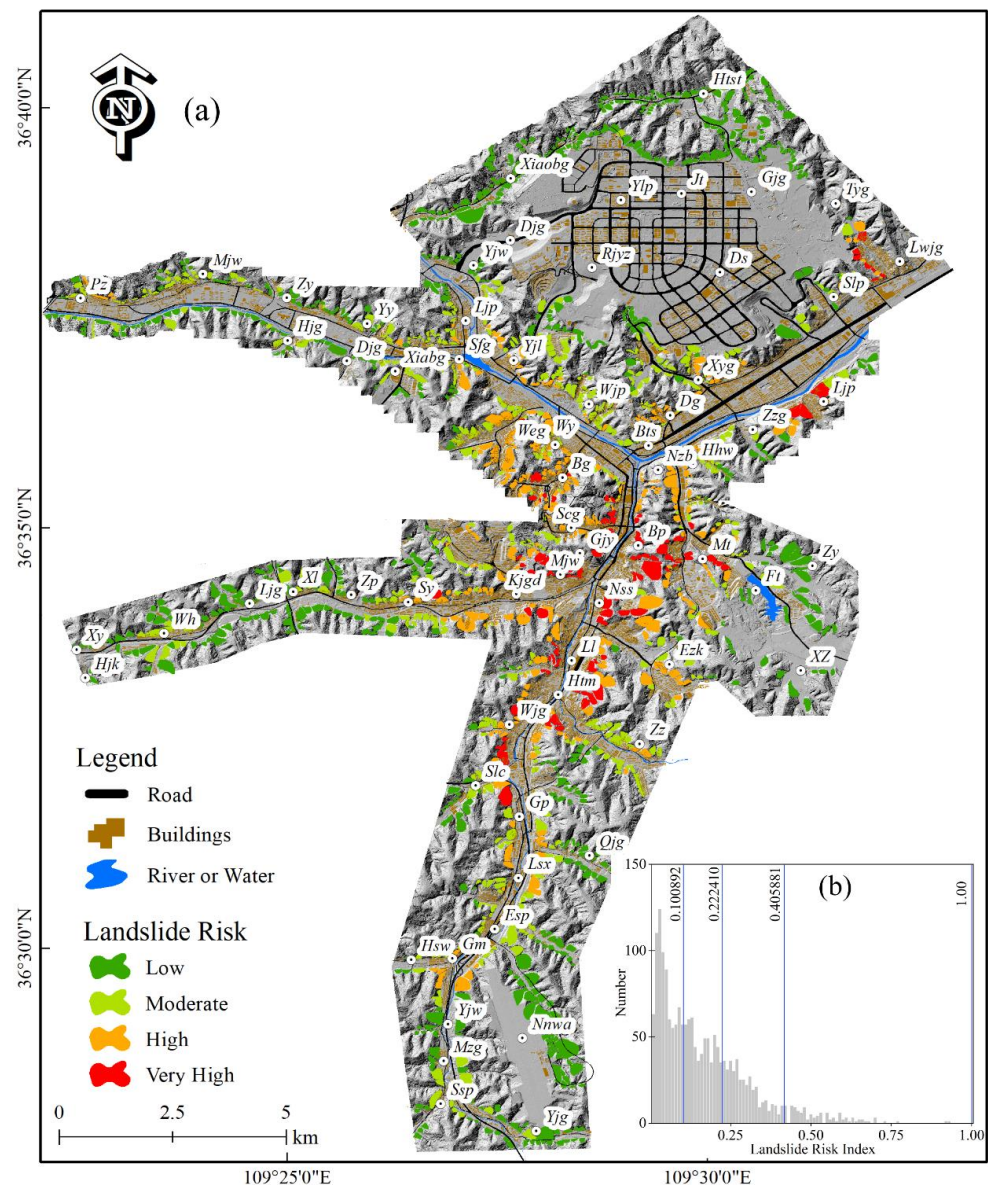
Figure 13. Landslide risk map of the study area in (**a**), and the distribution of the landslide risk index using the natural breaks in (**b**).

5. Discussion

Landslide risk assessment has been attracting the attention of researchers and governments in order to effectively deal with landslides in the study area. For this purpose, machine learning and DInSAR technology were used to evaluate the landslide susceptibility in the main urban parts of Yan'an City. Currently, the susceptibility, hazard, and risk of landslides in the whole of Yan'an City have been determined in existing studies. In terms of the methodology, they can be divided into the heuristic model and generalized objective functions based on experts' knowledge scoring [44,68,69], a quantitative model of evidence weight [42], and a physically deterministic model [43]. In terms of map units and scopes, they can be divided into grid cells (25 m or 30 m), catchment basin units [42–44,68,69], administrative boundaries [42–44], and watershed boundaries [68,69]. However, those results are not only subjective but also can only meet the needs of a wide range of risk management options and cannot truly reflect the geomorphic characteristics of the slope in the study area, which can be useful for risk management in a large administrative area. The research reviewed that an inventory including detailed landslide information and a rea-

sonable mapping unit as well as model type is a prerequisite for obtaining highly accurate assessment results [20]. Firstly, a landslide inventory with more detailed information can provide more input data to the model to analyze the relationship between landslides and geological environment factors to obtain a comprehensive landslide susceptibility map [70]. Some previous studies in the study area may not have shown this. Therefore, a complete landslide inventory, mapping all landslides in the study area, was determined through the interpretation of UAV images and site-by-site investigations. Secondly, field surveys and risk assessment of slope units on a large scale in small areas can provide planners with an adequate and applicable landslide risk map, especially in areas of critical concern such as urban centers. Research shows that grid cells or pixels are still the most commonly used map units in current papers on landslide assessment, and only a few papers have used slope units [20,21]. To reflect the geomorphic characteristics of slopes, slope units were used as map units in this study. Thirdly, the selection of a model is also an important factor affecting the accuracy of landslide susceptibility assessment. There are more and more models and methods developed for landslide susceptibility assessment, among which machine learning with good performance can be used to solve the nonlinear relationship between landslides and geological environment factors [16,34]. For this reason, random forest was selected to predict landslide susceptibility in the study area, with good proven performance [34,71]. Therefore, the accuracy of the landslide susceptibility assessment in this study was improved by using a machine learning model and slope units.

In addition, DInSAR technology was introduced in the process of hazard assessment to calculate slope deformation, and the hazard was calculated by giving the same weight coefficient of susceptibility and slope deformation. InSAR technology was used to perform a time-effective analysis, and the results can present the active state of slopes directly to predict the failure time and assess the hazard class of landslides [72,73]. At present, combining the ground deformation products from the InSAR technology with a landslide risk assessment map has become a concern in the relevant research [63,74]. However, many existing studies focus on the early identification and long-term monitoring of temporal and spatial evolution using InSAR technology [75,76] but there is still insufficient attention paid to risk assessment. The application of InSAR data in landslide risk assessment can improve the reliability of landslide predictions and make a reliable landslide risk map [45].

Finally, landslide risk was calculated by multiplying the hazard with the vulnerability composed of the spatial distribution and density of the buildings. The susceptibility, hazard, and risk assessment in this paper have a similar trend to the previous paper on Yan'an City in the area of different levels and spatial distributions [42–44], such as the area and percentage of low-susceptibility or hazard zones being greater than that of the higher-susceptibility or hazard zones, and the high-risk zones in the spatial distribution patterns are similar, which can also imply the accuracy of this work to a certain extent. Moreover, the risk assessment in this study can provide more specific guidance for risk management and prevention in practice.

There are some limitations that need to be considered in future research. Firstly, due to the lack of detailed population and property data, only the spatial location information of buildings was used for the vulnerability. The precondition for this question is to assume that the values of the buildings in the study area are the same, which would lead to certain information loss for vulnerability. Secondly, influenced by the observation mode of the radar satellites, the deformations obtained by the SAR images are ultimately along the LOS. However, the deformation rate along the slope (Vslope) can more intuitively reflect the real motion of the slopes, which can be transformed through the spatial geometric relationship between the radar LOS and slope. Due to the limitations of the image numbers in the SAR dataset from the study area, we have to use the ascending SAR images for InSAR processing, with which it is difficult to form an effective complement for the descending data. Therefore, we will also try to transform the LOS displacement into the slope direction displacement in future research. PSI or SBAS algorithms can be selected to obtain long-term ground deformation products if the SAR datasets have sufficient and long-term images,

which can reflect the long-term movement status and trend of slopes [63,74]. It is expected that more accurate risk assessment maps for the study or elsewhere could be produced by improving the above limitations.

6. Conclusions

Quantitative risk assessment is very effective for landslide risk management and urban areas need more detailed investigations and assessments. In this study, the quantitative landslide risk assessment was based on susceptibility and hazard assessments. The random forest classifier and eight environmental factors influencing landslides, including slope, profile curvature, relief, NDVI, landslides density, building density, the thickness of loess and the thickness of exposed bedrock were used to examine landslide susceptibility in Baota District, Yan'an City. Combined with DInSAR technology, landslide hazard mapping was developed to reflect the hazards quantitatively. Surface deformation, which can be caused by many factors (e.g., precipitation, slope groundwater, and engineering), can be detected by DInSAR technology with centimeter precision. Finally, the landslide risk map was obtained by being combined with the landslide susceptibility and hazard assessment and divided into very high-risk, high-risk, middle-risk, and low-risk areas according to the natural breaks method.

In this study, a total of 1841 slope units were mapped in the study area, including 334 landslides and 411 unstable slopes determined by field investigations, in which the main material of landslides and unstable slopes is loess and only a few of them contain bedrock. The length and width of landslides and unstable slopes are mainly between 50 m and 150 m, the slope angles are mainly between 20° and 50°, and the heights are predominantly between 30 and 90 m, where the slope angles and heights of most of the unstable slopes are larger than those of the landslides. The areas are usually less than 20×10^3 m^2. Reliable risk assessment was achieved using 1841 slope units, which were divided based on the terrain, optical images, and DEM. Remote sensing InSAR technology was applied to determine the quantitative landslide hazard zones. The classification results of the random forest classifier were evaluated with the receiver operating characteristics (ROC) curve and confusion matrix. The confusion matrix shows that the overall accuracy of the random forest classifier is 0.903 and that the AUC value is 0.96, with good prediction accuracy and classified ability of landslide susceptibility. The results of the landslide risk assessment indicate the risk level and the corresponding quantity of the slope units and total areas. Approximately 6% of the slope units located in the very high-risk zones and 20% of the slope units located in the high-risk zones must receive more attention to monitor the dynamics.

The present research has significant implications for landslide risk mitigation in Baota District, Yan'an City. Our scientific landslide risk map is expected to promote landslide prevention based on a zoning strategy and provide a valuable decision to support the local and regional government for disaster prevention, mitigation, and management, which eventually can effectively reduce the impacts of geohazards.

Author Contributions: Conceptualization, Y.Z.; methodology, W.L., Y.Z. and Y.L. (Yiwen Liang); software, W.L. and Y.L. (Yiwen Liang); validation, P.S., W.L., Y.Z. and Y.L. (Yiwen Liang); formal analysis, W.L. and Y.L. (Yiwen Liang); investigation, Y.L. (Yuanxi Li), X.S. and A.W.; resources, Y.Z.; data curation, Y.Z.; writing—original draft preparation, W.L. and Y.L. (Yiwen Liang); writing—review and editing, Y.Z. and X.M.; visualization, W.L. and Y.L. (Yiwen Liang); supervision, Y.Z. and X.M.; project administration, Y.Z.; funding acquisition, Y.Z. and X.M. All authors have read and agreed to the published version of the manuscript.

References

1. Froude, M.J.; Petley, D.N. Global fatal landslide occurrence from 2004 to 2016. *Nat. Hazards Earth Syst. Sci.* **2018**, *18*, 2161–2181. [CrossRef]
2. Xu, L.; Yan, D.; Zhao, T. Probabilistic evaluation of loess landslide impact using multivariate model. *Landslides* **2021**, *18*, 1011–1023. [CrossRef]
3. Peng, J.; Fan, Z.; Wu, D.; Zhuang, J.; Dai, F.; Chen, W.; Zhao, C. Heavy rainfall triggered loess–mudstone landslide and subsequent debris flow in Tianshui, China. *Eng. Geol.* **2015**, *186*, 79–90. [CrossRef]
4. Li, Y.; Wang, X.; Mao, H. Influence of human activity on landslide susceptibility development in the Three Gorges area. *Nat. Hazards* **2020**, *104*, 2115–2151. [CrossRef]
5. Fell, R.; Corominas, J.; Bonnard, C.; Cascini, L.; Leroi, E.; Savage, W.Z. Guidelines for landslide susceptibility, hazard and risk zoning for land use planning. *Eng. Geol.* **2008**, *102*, 85–98. [CrossRef]
6. Dai, F.C.; Lee, C.F.; Ngai, Y.Y. Landslide risk assessment and management: An overview. *Eng. Geol.* **2002**, *64*, 65–87. [CrossRef]
7. Huang, J.; Lyamin, A.V.; Griffiths, D.V.; Krabbenhoft, K.; Sloan, S.W. Quantitative risk assessment of landslide by limit analysis and random fields. *Comput. Geotech.* **2013**, *53*, 60–67. [CrossRef]
8. Tan, Q.; Bai, M.; Zhou, P.; Hu, J.; Qin, X. Geological hazard risk assessment of line landslide based on remotely sensed data and GIS. *Measurement* **2021**, *169*, 108370. [CrossRef]
9. Zhao, M.; Liu, X. Regional risk assessment for urban major hazards based on GIS geoprocessing to improve public safety. *Saf. Sci.* **2016**, *87*, 18–24. [CrossRef]
10. Trigila, A.; Iadanza, C.; Esposito, C.; Scarascia-Mugnozza, G. Comparison of Logistic Regression and Random Forests techniques for shallow landslide susceptibility assessment in Giampilieri (NE Sicily, Italy). *Geomorphology* **2015**, *249*, 119–136. [CrossRef]
11. Pourghasemi, H.R.; Rahmati, O. Prediction of the landslide susceptibility: Which algorithm, which precision? *Catena* **2018**, *162*, 177–192. [CrossRef]
12. Huang, F.; Yin, K.; Huang, J.; Gui, L.; Wang, P. Landslide susceptibility mapping based on self-organizing-map network and extreme learning machine. *Eng. Geol.* **2017**, *223*, 11–22. [CrossRef]
13. Godt, J.W.; Baum, R.L.; Savage, W.Z.; Salciarini, D.; Schulz, W.H.; Harp, E.L. Transient deterministic shallow landslide modeling: Requirements for susceptibility and hazard assessments in a GIS framework. *Eng. Geol.* **2008**, *102*, 214–226. [CrossRef]
14. Frattini, P.; Crosta, G.B.; Fusi, N.; Dal Negro, P. Shallow landslides in pyroclastic soils: A distributed modelling approach for hazard assessment. *Eng. Geol.* **2004**, *73*, 277–295. [CrossRef]
15. Pradhan, A.M.S.; Kim, Y.T. Evaluation of a combined spatial multi-criteria evaluation model and deterministic model for landslide susceptibility mapping. *Catena* **2016**, *140*, 125–139. [CrossRef]
16. Huang, F.; Cao, Z.; Guo, J.; Jiang, S.H.; Guo, Z. Comparisons of heuristic, general statistical and machine learning models for landslide susceptibility prediction and mapping. *Catena* **2020**, *191*, 104580. [CrossRef]
17. Yalcin, A. GIS-based landslide susceptibility mapping using analytical hierarchy process and bivariate statistics in Ardesen (Turkey): Comparisons of results and confirmations. *Catena* **2008**, *72*, 1–12. [CrossRef]
18. Zhu, A.; Miao, Y.; Wang, R.; Zhu, T.; Deng, Y.; Liu, J.; Yang, L.; Qin, C.; Hong, H. A comparative study of an expert knowledge-based model and two data-driven models for landslide susceptibility mapping. *Catena* **2018**, *166*, 317–327. [CrossRef]
19. Shu, H.; Hürlimann, M.; Molowny-Horas, R.; González, M.; Pinyol, J.; Abancó, C.; Ma, J. Relation between land cover and landslide susceptibility in Val d'Aran, Pyrenees (Spain): Historical aspects, present situation and forward prediction. *Sci. Total Environ.* **2019**, *693*, 133557. [CrossRef]
20. Reichenbach, P.; Rossi, M.; Malamud, B.; Mihir, M.; Guzzetti, F. A review of statistically-based landslide susceptibility models. *Earth Sci. Rev.* **2018**, *180*, 60–91. [CrossRef]
21. Pourghasemi, H.R.; Yansari, Z.T.; Panagos, P.; Pradhan, B. Analysis and evaluation of landslide susceptibility: A review on articles published during 2005–2016 (periods of 2005–2012 and 2013–2016). *Arab. J. Geosci.* **2018**, *11*, 193. [CrossRef]
22. Ramani, S.E.; Pitchaimani, K.; Gnanamanickam, V.R. GIS based landslide susceptibility mapping of Tevankarai Ar sub-watershed, Kodaikkanal, India using binary logistic regression analysis. *J. Mt. Sci. Engl.* **2011**, *8*, 505–517. [CrossRef]
23. Budimir, M.E.A.; Atkinson, P.M.; Lewis, H.G. A systematic review of landslide probability mapping using logistic regression. *Landslides* **2015**, *12*, 419–436. [CrossRef]
24. Khan, H.; Shafique, M.; Khan, M.A.; Bacha, M.A.; Shah, S.U.; Calligaris, C. Landslide susceptibility assessment using Frequency Ratio, a case study of northern Pakistan. *Egypt. J. Remote Sens. Space Sci.* **2019**, *22*, 11–24. [CrossRef]
25. Rabby, Y.W.; Li, Y. Landslide Susceptibility Mapping Using Integrated Methods: A Case Study in the Chittagong Hilly Areas, Bangladesh. *Geosciences* **2020**, *10*, 483. [CrossRef]

26. Neuhäuser, B.; Damm, B.; Terhorst, B. GIS-based assessment of landslide susceptibility on the base of the Weights-of-Evidence model. *Landslides* **2012**, *9*, 511–528. [CrossRef]

27. Kavzoglu, T.; Colkesen, I.; Sahin, E.K. Machine Learning Techniques in Landslide Susceptibility Mapping: A Survey and a Case Study. In *Landslides: Theory, Practice and Modelling*; Pradhan, S.P., Vishal, V., Singh, T.N., Eds.; Springer International Publishing: Cham, Switzerland, 2019; pp. 283–301. [CrossRef]

28. Ma, Z.; Mei, G.; Piccialli, F. Machine learning for landslides prevention: A survey. *Neural Comput. Appl.* **2021**, *33*, 10881–10907. [CrossRef]

29. Chen, X.; Chen, W. GIS-based landslide susceptibility assessment using optimized hybrid machine learning methods. *Catena* **2021**, *196*, 104833. [CrossRef]

30. Behnia, P.; Blais-Stevens, A. Landslide susceptibility modelling using the quantitative random forest method along the northern portion of the Yukon Alaska Highway Corridor, Canada. *Nat. Hazards* **2018**, *90*, 1407–1426. [CrossRef]

31. Hong, H.; Liu, J.; Bui, D.T.; Pradhan, B.; Acharya, T.D.; Pham, B.T.; Zhu, A.; Chen, W.; Ahmad, B.B. Landslide susceptibility mapping using J48 Decision Tree with AdaBoost, Bagging and Rotation Forest ensembles in the Guangchang area (China). *Catena* **2018**, *163*, 399–413. [CrossRef]

32. Goetz, J.N.; Brenning, A.; Petschko, H.; Leopold, P. Evaluating machine learning and statistical prediction techniques for landslide susceptibility modeling. *Comput. Geosci.* **2015**, *81*, 1–11. [CrossRef]

33. Xie, Z.; Chen, G.; Meng, X.; Zhang, Y.; Qiao, L.; Tan, L. A comparative study of landslide susceptibility mapping using weight of evidence, logistic regression and support vector machine and evaluated by SBAS-InSAR monitoring: Zhouqu to Wudu segment in Bailong River Basin, China. *Environ. Earth Sci.* **2017**, *76*, 313. [CrossRef]

34. Chen, W.; Xie, X.; Wang, J.; Pradhan, B.; Hong, H.; Bui, D.T.; Duan, Z.; Ma, J. A comparative study of logistic model tree, random forest, and classification and regression tree models for spatial prediction of landslide susceptibility. *Catena* **2017**, *151*, 147–160. [CrossRef]

35. Huang, F.; Ye, Z.; Jiang, S.; Huang, J.; Chang, Z.; Chen, J. Uncertainty study of landslide susceptibility prediction considering the different attribute interval numbers of environmental factors and different data-based models. *Catena* **2021**, *202*, 105250. [CrossRef]

36. Guzzetti, F.; Carrara, A.; Cardinali, M.; Reichenbach, P. Landslide hazard evaluation: A review of current techniques and their application in a multi-scale study, Central Italy. *Geomorphology* **1999**, *31*, 181–216. [CrossRef]

37. Erener, A.; Düzgün, H.S.B. Landslide susceptibility assessment: What are the effects of mapping unit and mapping method? *Environ. Earth Sci.* **2012**, *66*, 859–877. [CrossRef]

38. Jacobs, L.; Kervyn, M.; Poesen, J.; Reichenbach, P.; Rossi, M.; Marchesini, I.; Alvioli, M.; Dewitte, O. Dealing with heterogeneous landslide information for landslide susceptibility assessment: Comparing a pixel-based and slope unit-based approach. In Proceedings of the EGU General Assembly Conference, Vienna, Austria, 23–28 April 2017; p. 6260.

39. Ba, Q.; Chen, Y.; Deng, S.; Yang, J.; Li, H. A comparison of slope units and grid cells as mapping units for landslide susceptibility assessment. *Earth Sci. Inform.* **2018**, *11*, 373–388. [CrossRef]

40. Jacobs, L.; Kervyn, M.; Reichenbach, P.; Rossi, M.; Marchesini, I.; Alvioli, M.; Dewitte, O. Regional susceptibility assessments with heterogeneous landslide information: Slope unit- vs. pixel-based approach. *Geomorphology* **2020**, *356*, 107084. [CrossRef]

41. Peng, J.; Wang, Q.; Zhuang, J.; Leng, Y.; Fan, Z.; Wang, S. Dynamic formation mechanism of landslide disaster on the Loess Plateau. *J. Geomech.* **2020**, *26*, 714–730. [CrossRef]

42. Xue, Q.; Zhang, M.; Li, L. Loess landslide susceptibility evaluation based on slope unit and information value method in Baota District, Yan' an. *Geol. Bull. China* **2015**, *34*, 118–125.

43. Gao, B.; Wang, X. Risk Zoning of Landslide Based on SINMAP Model in Yan'an City. *Bull. Soil Water Conserv.* **2019**, *39*, 211–216. (In Chinese) [CrossRef]

44. Yang, L.; Mou, X.; Li, C.; Zheng, X.; Yue, D. Risk assessment of geological hazards in Baota District, Yan' an City, Shanxi, China. *Mt. Res.* **2020**, *38*, 679–690. [CrossRef]

45. Ciampalini, A.; Raspini, F.; Lagomarsino, D.; Catani, F.; Casagli, N. Landslide susceptibility map refinement using PSInSAR data. *Remote Sens. Environ.* **2016**, *184*, 302–315. [CrossRef]

46. Ma, R. Analysis of trend and mutation characteristics of precipitation in yan'an city during past 45 years. *J. Yanan Univ. Nat. Sci. Ed.* **2016**, *35*, 95–99. [CrossRef]

47. Zhu, J.; Chen, Z.; Zhu, Y. Distribution Regularity and Development Characteristics of Landslides in Yan'an. *Geol. Sci. Technol. Inf.* **2017**, *36*, 236–243. [CrossRef]

48. Van Westen, C.J.; Castellanos, E.; Kuriakose, S.L. Spatial data for landslide susceptibility, hazard, and vulnerability assessment: An overview. *Eng. Geol.* **2008**, *102*, 112–131. [CrossRef]

49. Sharma, R.H. Evaluating the effect of slope curvature on slope stability by a numerical analysis. *Aust. J. Earth Sci.* **2013**, *60*, 283–290. [CrossRef]

50. Tang, Y.; Feng, F.; Guo, Z.; Feng, W.; Li, Z.; Wang, J.; Sun, Q.; Ma, H.; Li, Y. Integrating principal component analysis with statistically-based models for analysis of causal factors and landslide susceptibility mapping: A comparative study from the loess plateau area in Shanxi (China). *J. Clean. Prod.* **2020**, *277*, 124159. [CrossRef]

51. Ho, J.Y.; Lee, K.T.; Chang, T.C.; Wang, Z.Y.; Liao, Y.H. Influences of spatial distribution of soil thickness on shallow landslide prediction. *Eng. Geol.* **2012**, *124*, 38–46. [CrossRef]

52. Zhang, M.; Tan, X.; Dong, Y.; Sun, P.; Dong, P.; Lu, N. Initial analysis on environmental effect of cutting hills to backfill ditch project on Loess Plateau—Take Yan' an New District as an example. *Geol. Rev.* **2019**, *65*, 1409–1421. [CrossRef]

53. Aksu, G.; Güzeller, C.; Eser, T. The Effect of the Normalization Method Used in Different Sample Sizes on the Success of Artificial Neural Network Model. *Int. J. Assess. Tools Educ.* **2019**, *6*, 170–192. [CrossRef]

54. Colesanti, C.; Wasowski, J. Investigating landslides with space-borne Synthetic Aperture Radar (SAR) interferometry. *Eng. Geol.* **2006**, *88*, 173–199. [CrossRef]

55. Wegmüller, U.; Strozzi, T.; Tosi, L. Differential SAR interferometry for land subsidence monitoring: Methodology and examples. In Proceedings of the Sixth International Symposium on Land Subsidence, Ravenna, Italy, 24–29 September 2000.

56. Pasquali, P.; Pellegrini, R.; Prati, C.; Rocca, F. Combination of interferograms from ascending and descending orbits. In Proceedings of the IGARSS '94—1994 IEEE International Geoscience and Remote Sensing Symposium, Pasadena, CA, USA, 8–12 August 1994; Volume 2, pp. 733–735.

57. Yu, X.; Xue, D.; Chen, F. Analysis of Influence of Vegetation Coverage and Slope on SAR Interferometric Coherence. *Mt. Res.* **2020**, *38*, 926–934. [CrossRef]

58. Breiman, L. Random Forests. *Mach. Learn.* **2001**, *45*, 5–32. [CrossRef]

59. Wu, Q.; Jia, C.; Chen, S.; Li, H. SBAS-InSAR Based Deformation Detection of Urban Land, Created from Mega-Scale Mountain Excavating and Valley Filling in the Loess Plateau: The Case Study of Yan'an City. *Remote Sens.* **2019**, *11*, 1673. [CrossRef]

60. Liao, M.; Zhang, R.; Lv, J.; Yu, B.; Pang, J.; Li, R.; Xiang, W.; Tao, W. Subsidence Monitoring of Fill Area in Yan'an New District Based on Sentinel-1A Time Series Imagery. *Remote Sens.* **2021**, *13*, 3044. [CrossRef]

61. Chen, W.; Pourghasemi, H.R.; Panahi, M.; Kornejady, A.; Wang, J.; Xie, X.; Cao, S. Spatial prediction of landslide susceptibility using an adaptive neuro-fuzzy inference system combined with frequency ratio, generalized additive model, and support vector machine techniques. *Geomorphology* **2017**, *297*, 69–85. [CrossRef]

62. Zhao, F.; Meng, X.; Zhang, Y.; Chen, G.; Su, X.; Yue, D. Landslide Susceptibility Mapping of Karakorum Highway Combined with the Application of SBAS-InSAR Technology. *Sensors* **2019**, *19*, 2685. [CrossRef]

63. Lu, P.; Catani, F.; Tofani, V.; Casagli, N. Quantitative hazard and risk assessment for slow-moving landslides from Persistent Scatterer Interferometry. *Landslides* **2014**, *11*, 685–696. [CrossRef]

64. Hammad, M.; Van Leeuwen, B.; Mucsi, L. Integration of gis and advanced remote sensing techniques for landslide hazard assessment: A case study of northwest syria. *ISPRS Ann. Photogramm. Remote Sens. Spat. Inf. Sci.* **2020**, *VI-3/W1-2020*, 27–34. [CrossRef]

65. Saaty, T.L. Multicriteria decision making: The analytic hierarchy process: Planning, priority setting resource allocation. *Resour. Alloc.* **1990**, *2*, 1–20.

66. Frédéric, L.; Asté, J.; Leroi, E. Vulnerability assessment of elements exposed to mass-movement: Working toward a better risk perception. In *Landslides-Glissements de Terrain*; Balkema: Rotterdam, The Netherlands, 1996; pp. 263–270.

67. Akgun, A.; Kıncal, C.; Pradhan, B. Application of remote sensing data and GIS for landslide risk assessment as an environmental threat to Izmir city (west Turkey). *Environ. Monit. Assess.* **2012**, *184*, 5453–5470. [CrossRef] [PubMed]

68. Tang, Y.; Xue, Q.; Li, Q.; Sun, P. Slope classification system for loess collapse risk assessment. *J. Eng. Geol.* **2012**, *20*, 378–386.

69. Tang, Y.; Zhang, M.; Xue, Q. Landslide risk assessment methods and flow on a large scale—A case study of loess landslides risk assessment in Yan'an urban districts, Shaanxi, China. *Geol. Bull. China* **2011**, *30*, 166–172.

70. Galli, M.; Ardizzone, F.; Cardinali, M.; Guzzetti, F.; Reichenbach, P. Comparing landslide inventory maps. *Geomorphology* **2008**, *94*, 268–289. [CrossRef]

71. Youssef, A.M.; Pourghasemi, H.R. Landslide susceptibility mapping using machine learning algorithms and comparison of their performance at Abha Basin, Asir Region, Saudi Arabia. *Geosci. Front.* **2021**, *12*, 639–655. [CrossRef]

72. Zhang, Y.; Meng, X.; Novellino, A.; Dijkstra, T.; Chen, G.; Jordan, C.; Li, Y.; Su, X. Characterization of pre-failure deformation and evolution of a large earthflow using InSAR monitoring and optical image interpretation. *Landslides* **2021**, *19*, 35–50. [CrossRef]

73. Confuorto, P.; Medici, C.; Bianchini, S.; Del Soldato, M.; Rosi, A.; Segoni, S.; Casagli, N. Machine Learning for Defining the Probability of Sentinel-1 Based Deformation Trend Changes Occurrence. *Remote Sens.* **2022**, *14*, 1748. [CrossRef]

74. Ambrosi, C.; Strozzi, T.; Scapozza, C.; Wegmüller, U. Landslide hazard assessment in the Himalayas (Nepal and Bhutan) based on Earth-Observation data. *Eng. Geol.* **2018**, *237*, 217–228. [CrossRef]

75. Mondini, A.C.; Guzzetti, F.; Chang, K.; Monserrat, O.; Martha, T.R.; Manconi, A. Landslide failures detection and mapping using Synthetic Aperture Radar: Past, present and future. *Earth Sci. Rev.* **2021**, *216*, 103574. [CrossRef]

76. Kang, Y.; Lu, Z.; Zhao, C.; Xu, Y.; Kim, J.; Gallegos, A.J. InSAR monitoring of creeping landslides in mountainous regions: A case study in Eldorado National Forest, California. *Remote Sens. Environ.* **2021**, *258*, 112400. [CrossRef]